Mechanisms controlling dissolved iron distribution in the North Pacific: A model study

K. Misumi,[1,2] D. Tsumune,[1] Y. Yoshida,[1] K. Uchimoto,[3] T. Nakamura,[3] J. Nishioka,[3] H. Mitsudera,[3] F. O. Bryan,[2] K. Lindsay,[2] J. K. Moore,[4] and S. C. Doney[5]

Received 2 September 2010; revised 1 April 2011; accepted 14 April 2011; published 22 July 2011.

[1] Mechanisms controlling the dissolved iron distribution in the North Pacific are investigated using the Biogeochemical Elemental Cycling (BEC) model with a resolution of approximately 1° in latitude and longitude and 60 vertical levels. The model is able to reproduce the general distribution of iron as revealed in available field data: surface concentrations are generally below 0.2 nM; concentrations increase with depth; and values in the lower pycnocline are especially high in the northwestern Pacific and off the coast of California. Sensitivity experiments changing scavenging regimes and external iron sources indicate that lateral transport of sedimentary iron from continental margins into the open ocean causes the high concentrations in these regions. This offshore penetration only appears under a scavenging regime where iron has a relatively long residence time at high concentrations, namely, the order of years. Sedimentary iron is intensively supplied around continental margins, resulting in locally high concentrations; the residence time with respect to scavenging determines the horizontal scale of elevated iron concentrations. Budget analysis for iron reveals the processes by which sedimentary iron is transported to the open ocean. Horizontal mixing transports sedimentary iron from the boundary into alongshore currents, which then carry high iron concentrations into the open ocean in regions where the alongshore currents separate from the coast, most prominently in the northwestern Pacific and off of California.

Citation: Misumi, K., et al. (2011), Mechanisms controlling dissolved iron distribution in the North Pacific: A model study, *J. Geophys. Res.*, *116*, G03005, doi:10.1029/2010JG001541.

1. Introduction

[2] Iron is an essential nutrient for marine phytoplankton because of its role in various metabolic reactions and enzymes [*Morel and Price*, 2003; *Barbeau*, 2006]. Iron deficiency limits primary production in the "high-nutrient, low-chlorophyll" (HNLC) regions: the subarctic North Pacific, equatorial Pacific and Southern Ocean [*Martin and Fitzwater*, 1988; *Martin et al.*, 1990, 1994], and also indirectly controls the production in the nitrogen-limited subtropics by limiting N_2 fixation [*Michaels et al.*, 1996; *Falkowski*, 1997; *Falkowski et al.*, 1998; *Berman-Frank et al.*, 2001; *Morel and Price*, 2003; *Kustka et al.*, 2003; *Mills et al.*, 2004; *Moore and Doney*, 2007]. Thus, iron is regarded as a key element for understanding the marine carbon cycle. However, the iron distribution and cycle in the ocean are not well established owing to the analytical difficulty of measuring iron and its complex chemical nature in seawater.

[3] A growing body of field data on dissolved iron concentrations is improving our understanding of the ocean distribution of iron and is guiding the development of iron cycle models. *Johnson et al.* [1997] compiled field data in the North Pacific and additional data from the Southern Ocean and North Atlantic. The data exhibited a nutrient-type vertical profile with concentrations in the deep water roughly converging to 0.6 nM without significant interocean differences. Based on these observations, they proposed an iron cycle model where complexation by strong iron-binding ligands reduces iron scavenging rates at concentrations less than a presumed ligand concentration of 0.6 nM. *Lefevre and Watson* [1999] incorporated this iron model into a 10-box ocean model; the results demonstrated that complexation is essential to explain the observed deep ocean homogeneous iron distribution. *Archer and Johnson* [2000] introduced explicit kinetics for iron and the binding ligands and incorporated it into a three-dimensional general circulation model (GCM); the results confirmed the importance of the iron complexation. Alternatively, *Boyle* [1997] and *Lefevre and*

[1]Environmental Science Research Laboratory, Central Research Institute of Electric Power Industry, Abiko, Japan.
[2]Climate and Global Dynamics Division, National Center for Atmospheric Research, Boulder, Colorado, USA.
[3]Pan-Okhotsk Research Center, Institute of Low Temperature Science, Hokkaido University, Sapporo, Japan.
[4]Department of Earth System Science, University of California, Irvine, California, USA.
[5]Department of Marine Chemistry and Geochemistry, Woods Hole Oceanographic Institution, Woods Hole, Massachusetts, USA.

0148-0227/11/2010JG001541

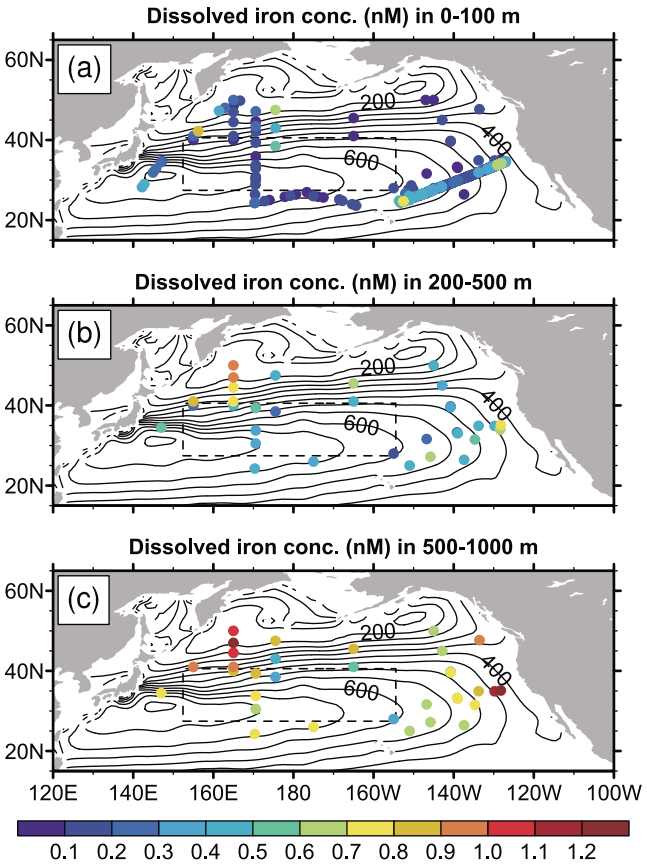

Figure 1. Horizontal distribution of dissolved iron concentrations (nM) in field data (compiled by *Moore and Braucher* [2008]): averaged in the (a) surface (0–100 m), (b) upper pycnocline (200–500 m) and (c) lower pycnocline (500–1000 m), respectively. Data within 500 km of the coast are eliminated. Contour lines are depth (in meters) of 26.8 σ_θ isopycnal surface calculated from the World Ocean Atlas climatology 2005 [*Locarnini et al.*, 2006]. A box region enclosed by dotted line is referred to as the central North Pacific in section 3.

Watson [1999] noted that the apparent constancy of the deep dissolved iron distribution is possibly attributable to the limited number of observations available at that time.

[4] Further accumulation of field data has revealed interocean gradients of dissolved iron concentrations [*de Baar and de Jong*, 2001; *Gregg et al.*, 2003; *Parekh et al.*, 2005; *Moore and Braucher*, 2008]. The concentrations in the North Atlantic and Arabian Sea are high even in surface waters [*Vink and Measures*, 2001; *Measures and Vink*, 1999]. The surface concentrations in both the North Pacific and Southern Ocean are usually below 0.2 nM in the open ocean, but the subsurface concentrations are higher in the North Pacific, typically 0.6 nM, than those in the Southern Ocean, typically 0.3 nM [*Moore and Braucher*, 2008].

[5] Model studies have suggested that the rate and functional form of iron scavenging play an important role in the governing of interocean gradients of dissolved iron concentrations. *Parekh et al.* [2004] conducted box-model experiments to explore a large parameter space for iron scavenging. The result showed that the "single-ligand" parameterization proposed by *Archer and Johnson* [2000] reproduces the lower iron concentrations in the Southern Ocean than in the North Pacific if relatively high iron-binding ligand concentrations and low conditional stability constants are used in the parameterization. Using these scavenging parameters, the scavenging rates are moderately high even for iron concentrations below the ligand concentration. Such a scavenging regime allows dissolved iron to be more spatially variable and reproduces the lower concentrations in the Southern Ocean. *Parekh et al.* [2005] incorporated the iron model and optimized parameters into a GCM and successfully simulated the lower concentrations in the deep Southern Ocean.

[6] Spatial distributions of external iron sources also have been considered to contribute to the interocean concentration gradients. Most early studies assumed that aeolian dust is the dominant iron source to the open ocean [*Duce and Tindale*, 1991; *Fung et al.*, 2000]. Continental margin sediments have recently been regarded as an important iron source [*Elrod et al.*, 2004]. Both the aeolian and sedimentary sources are now incorporated into a number of numerical models [*Moore et al.*, 2004; *Aumont and Bopp*, 2006; *Moore and Braucher*, 2008; *Parekh et al.*, 2008]. Sensitivity experiments either prescribing aeolian or sedimentary sources alone have suggested that sedimentary iron contributes to some open ocean regions, particularly in the North Pacific [*Moore and Braucher*, 2008]. A recent GCM study indicated that hydrothermal sources could influence the iron distribution, especially in the deep Southern Hemisphere oceans [*Tagliabue et al.*, 2010].

[7] The relative abundance of field data in the North Pacific has established the existence of concentration gradients within that basin. *Nishioka et al.* [2007] showed field data along a cross section at 165°E that exhibited a high iron concentration core centered on 48°N with the maximum concentration over 1 nM around 1000 m depth. The high concentrations extend to the subtropical region through the density range of the North Pacific intermediate water (NPIW; 26.6–27.5σ_θ [i.e., *Yasuda et al.*, 2001]). They indicated that ventilation of the intermediate water exports sedimentary iron from the continental shelf of the Okhotsk Sea into the North Pacific. In contrast to the 165°E section, a section along 140°W [*Johnson et al.*, 1997] does not show such a high concentration core. The concentrations in the eastern subarctic region are roughly 0.6 nM in the lower pycnocline, and are roughly one third lower than those in the western subarctic region. The west-east gradient has been reported by some other studies [*Nishioka et al.*, 2003; *Takata et al.*, 2006]. In addition, the concentrations in the lower pycnocline of the eastern section are slightly higher in the subtropical region compared to the subarctic region. The higher concentrations in the subtropics are attributed to offshore sedimentary iron transport; the offshore penetration from the coastal region to the open ocean is seen in a zonal cross section along 33°N [*Johnson et al.*, 1997].

[8] We can summarize the features of iron distribution in the North Pacific from the compiled data (Figure 1). The concentrations in the surface water are generally below 0.2 nM in the open ocean and tend to increase with depth, indicating a nutrient type vertical profile. The concentrations in the upper and lower pycnocline (Figures 1b and 1c) show high concentrations in the northwestern region and off the

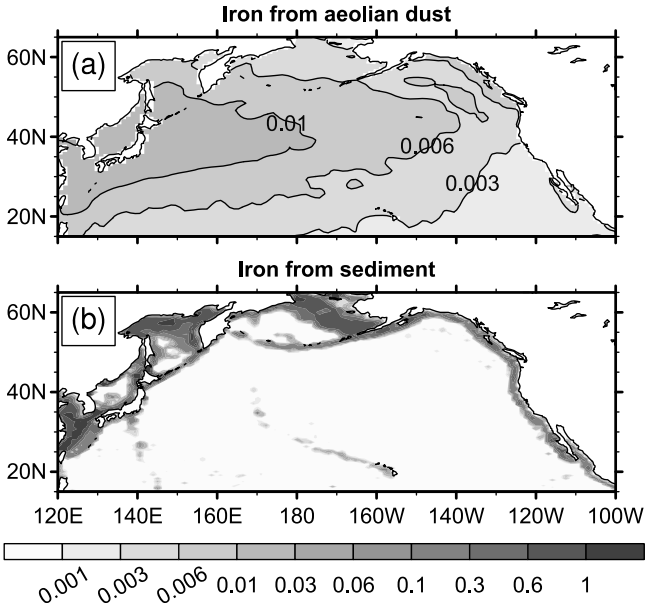

Figure 2. External iron inputs (mmol m^{-2}) from (a) aeolian dust [*Luo et al.*, 2003] and (b) seafloor sediments [*Moore and Braucher*, 2008] in the North Pacific.

coast of California, implying a contribution of sedimentary iron sources in these regions. The lower pycnocline concentrations in these areas exceed 1 nM even in the open ocean, and concentrations in other areas are roughly 0.6 nM on average. The structure of the spatial concentration variation in the upper and lower pycnocline differs from any estimated distributions of major external iron sources, implying that internal processes in the ocean significantly affect the distribution. However, the detailed mechanisms controlling the iron distribution in the North Pacific have not been fully established.

[9] This study examines factors controlling the basin scale iron distribution in the North Pacific through numerical experimentation. We conduct a suite of numerical experiments changing the iron scavenging parameterization and iron sources using a state-of-the-art marine biogeochemical model, with an explicit representation of the iron cycle. The results reveal that offshore transport of sedimentary iron is especially large in the northwestern Pacific and off the coast of California because the currents are favorable for transporting sedimentary iron to the open ocean. In section 2, we describe our model and experimental design. In section 3, we show the results of experiments changing iron scavenging and external iron sources. In section 4, we propose a plausible iron scavenging regime for the North Pacific and discuss sedimentary iron transport processes. In section 5, we conclude with a summary on sedimentary iron transport in the North Pacific.

2. Model and Experimental Design

2.1. Model

[10] We use the Biogeochemical Elemental Cycling (BEC) model [*Moore et al.*, 2004; *Moore and Braucher*, 2008] embedded in the ocean component of the Community Climate System Model (CCSM3.5). The BEC model is run within the Parallel Ocean Program (POP) [*Smith and Gent*, 2004; *Collins et al.*, 2006]; the other components of the CCSM, that is atmosphere, land and sea ice models, are not coupled in the calculation in this study.

[11] The POP model is a z coordinate, primitive equation model with a global domain. The model resolution is 1.125° in longitude, 0.27° to 0.64° in latitude, and 60 vertical levels varying in thickness from 10 m at the surface to 250 in the abyss. The model uses a curvilinear horizontal mesh; its northern pole is translated to Greenland. The difference of the physical model configurations and parameterizations from the CCSM3.0 version [*Danabasoglu et al.*, 2006] is summarized by *Yeager and Jochum* [2009].

[12] The BEC model simulates upper ocean ecosystem dynamics [*Moore et al.*, 2004; *Moore and Braucher*, 2008] and full-depth biogeochemistry [*Doney et al.*, 2006]. The skill of the BEC simulated ecology and biogeochemistry was assessed in two recent studies [*Doney et al.*, 2009a, 2009b]. The model considers four classes of phytoplankton functional type: pico/nano-plankton, coccolithophores, diatoms and diazotrophs; one class of zooplankton; five nutrients: dissolved nitrate, ammonia, phosphorus, iron and silicate; carbonate geochemistry and oxygen cycling.

[13] The BEC model considers three classes of iron: total dissolved iron (dFe; referred to as "dissolved iron" hereafter), dissolved organic iron (DOFe) and particulate iron (PFe). The dFe class represents soluble and colloidal forms of iron (so-called free dissolved iron dFe′) and iron complexed with iron-binding ligands; this is the sole iron class utilized by phytoplankton. In addition to biological uptake, dissolved iron is subject to particle scavenging. The rate of particle scavenging is parameterized as a function of the total dissolved iron concentration dFe as follows [*Moore and Braucher*, 2008]:

$$scav = -Sc \times dFe \tag{1}$$

$$Sc = Sc_b \qquad (\text{where } dFe < L) \tag{2}$$

$$Sc = Sc_b + (dFe - L) \times C_{high} \qquad (\text{where } dFe \geq L) \tag{3}$$

$$Sc_b = Fe_b \times (6 \times sPOC + sDust + sbSi + sCaCO_3), \tag{4}$$

where $scav$ is the dissolved iron tendency owing to scavenging; Sc is scavenging rate; Sc_b is base scavenging rate; L is a parameter representing the total ligand concentration; C_{high} is a proportionality constant; Fe_b is a parameter of the base scavenging coefficient that represents affinity of dissolved iron to sinking particles; $sPOC$, $sDust$, $sbSi$ and $sCaCO_3$ are sinking particle fluxes for particulate organic matter, aeolian dust, biogenic silica and calcium carbonate, respectively.

[14] Iron scavenging increases nonlinearly with total dissolved iron concentration dFe, and the shape of the scavenging to dFe curve is qualitatively similar to parameterizations based on free dissolved iron concentration dFe′ (see section 4.1 and Appendix A). The BEC model implicitly takes into account ligand kinetics by increasing the scavenging rate where the dFe concentrations exceed a presumed ligand concentration (equation (3)). Comparison of the BEC

Table 1. Experimental Case in This Study[a]

Case Name	Scavenging Parameters		Iron Sources	
	L	Fe_b	Dust	Sediment
MB2008	1 (=0.6 nM)	1 (=0.00384 ng^{-1} cm^{-1})	on	on
BEST-FIT	2	1	on	on
WEAK-BINDING	1	0.5	on	on
MB2008 Dust Only	1	1	on	off
MB2008 Sediment Only	1	1	off	on
BEST-FIT Dust Only	2	1	on	off
BEST-FIT Sediment Only	2	1	off	on

[a]The values in scavenging parameters are described in multiples from the values used by *Moore and Braucher* [2008]. Scavenging parameters of "L" and "Fe_b" represent the total ligand concentration and the base scavenging coefficient, respectively. The horizontal distributions of external iron sources are in Figure 2.

iron scavenging parameterization (equations (1)–(4)) with the "single-ligand" approach [*Archer and Johnson*, 2000; *Parekh et al.*, 2005; *Doney et al.*, 2006; *Aumont and Bopp*, 2006] is described in Appendix A.

[15] Without better constraints from field data, we assume that L is temporally and spatially constant. We conduct sensitivity experiments with different scavenging regimes by changing L and Fe_b; details are described below. The model puts 90% of scavenged iron to PFe, and the remaining 10% is instantaneously removed from the ocean supposing transformation to insoluble form. *Moore and Braucher* [2008] assumed that 6% of iron sorbed to sinking particles desorbs per 100 m sinking. Here, we arbitrarily increase the fraction to 24% because the model tends to underestimate dFe concentrations below the pycnocline of the Pacific [*Moore and Braucher*, 2008].

[16] We consider two iron sources to the ocean, aeolian dust and seafloor sediments (Figure 2). We assume that aeolian dust contains a constant fraction of iron (3.5 weight %). A small fraction, 2%, of the dust iron instantaneously dissolves at the sea surface. The remaining dust iron enters the pool of sinking particles partitioned into "soft" (3%) and "hard" (97%) fractions with remineralization length scales of 600 m and 120,000 m, respectively; as a result 6% of the dust iron deposited to the ocean is remineralized over a 4000 m water column [*Moore and Braucher*, 2008]. Iron supplied from seafloor sediments is estimated based on *Elrod et al.* [2004] where iron release from sediments is assumed to be proportional to organic carbon oxidation in the sediments. For additional details, the reader is referred to *Moore and Braucher* [2008]. Hydrothermal sources of iron are not considered in our calculation, but the impact will be small above 1000 m in the North Pacific where we focus in this study [*Tagliabue et al.*, 2010].

2.2. Experimental Design

[17] We spun up the model for 120 years with the same scavenging parameters as used by *Moore and Braucher* [2008], and then conducted a suite of experiments with different scavenging regimes and iron sources (Table 1). In case "MB2008," we keep the same scavenging parameters as *Moore and Braucher* [2008], L = 0.6 nM and Fe_b = 0.00384 cm^2 ng^{-1}, respectively. In case "BEST-FIT," we increase L by a factor of two, supposing a scavenging regime with relatively plentiful iron-binding ligands; this case best fits the North Pacific field data. In case "WEAK-BINDING," Fe_b is multiplied by a factor of 0.5, supposing a scavenging regime where iron has a weak affinity to sinking particles. We additionally conduct experiments denoted by "Dust Only" and "Sediment Only" where the model is run with either aeolian or sedimentary sources alone. In all cases, the model is further integrated for 50 years from the end of the 120 year spin-up calculation. The simulated dissolved iron fields have reasonably small drifts in the upper 1000 m (i.e., the tendencies of annual mean dissolved iron concentrations averaged over the North Pacific at 1000 m depth are less than 0.002 nM yr^{-1} for all cases). We focus on the results for the upper 1000 m from the last year of each experiment.

[18] The initial conditions for temperature and salinity are from Polar Science Center Hydrographic Climatology 2 [*Steele et al.*, 2001]; those for macronutrients are from World Ocean Atlas 1998 [*Conkright et al.*, 1998] and for inorganic carbon and alkalinities are from the preindustrial values of the Global Data Analysis Project (GLODAP [*Key et al.*, 2004]). For dissolved iron, we use a result from a 3000 year simulation with a lower resolution version of the BEC model [*Moore and Doney*, 2007]. Atmospheric CO_2 concentration is set to the preindustrial value (289 ppm). The sea surface forcing is from a synthetic, repeating "normal year" forcing [*Large and Yeager*, 2004]: 6-hourly atmospheric state data based on NCEP reanalysis [*Kalnay et al.*, 1996], daily satellite radiation data [*Zhang et al.*, 2004], monthly precipitation from *Xie and Arkin* [1996] and the Global Precipitation Climatology Project (GPCP [*Huffman et al.*, 1997]).

[19] The ventilation of NPIW was poorly simulated in the 120 year spin-up calculation. This ventilation process needs to be reasonably simulated because it is considered to play an important role in sedimentary iron transport in the North Pacific [*Nishioka et al.*, 2007]. To ameliorate the ventilation issues, we modified the model configuration around the Okhotsk Sea at the beginning of the sensitivity experiments. We restored simulated salinities to the field data [*Shcherbina et al.*, 2003] for the northern shelf of the Okhotsk Sea to reflect the effect of brine rejection. The transport of the East Sakhalin Current, a southward western boundary current in the Okhotsk Sea [*Ohshima et al.*, 2004], was too weak; therefore we intensified wind speeds by a factor of 1.5 over the Okhotsk Sea. In addition, we enhanced vertical diffusivities around the Kuril Islands to represent the effects of strong tidal mixing around the islands [*Nakamura and Awaji*, 2004; *Nakamura et al.*, 2006]. These changes have been shown to improve the simulation of ventilation of NPIW [*Uchimoto et al.*, 2011].

3. Results

3.1. Horizontal Distribution

[20] The simulated dissolved iron concentrations in the surface water are generally below 0.2 nM in the MB2008 and BEST-FIT cases and are slightly higher in the WEAK-BINDING case (Figures 3a–3c). The results are similar among the cases and are consistent with the field data. The

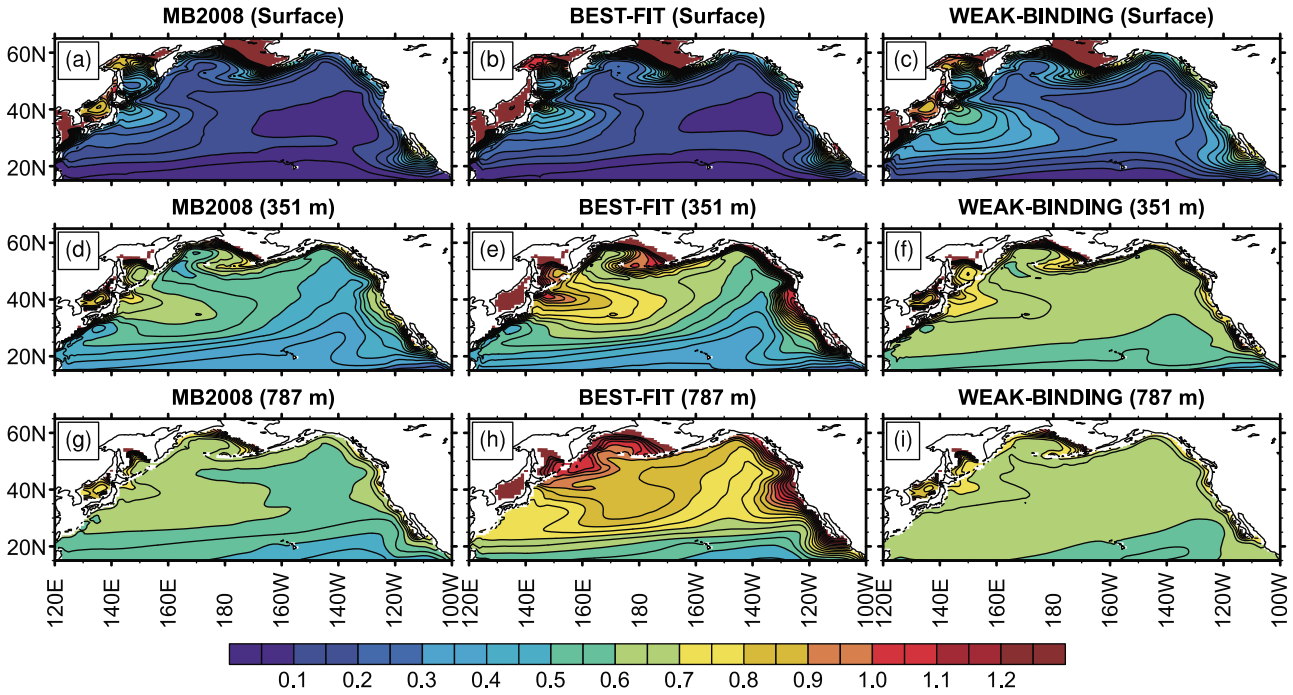

Figure 3. Horizontal distribution of the simulated dissolved iron concentrations (nM): in the surface for the (a) MB2008, (b) BEST-FIT and (c) WEAK-BINDING cases; at 351 m depth for the (d) MB2008, (e) BEST-FIT and (f) WEAK-BINDING cases; at 787 m depth for the (g) MB2008, (h) BEST-FIT and (i) WEAK-BINDING cases, respectively.

insensitivity to the scavenging regimes is because biological uptake strongly controls the concentrations in surface waters.

[21] In the upper pycnocline (Figures 3d–3f), the concentrations in the MB2008 case are relatively high in the northwestern region and off the coast of California; the overall pattern is consistent with the field data (Figure 1b). However, the MB2008 case underestimates iron levels in regions with high concentrations in the field data. Both the BEST-FIT and WEAK-BINDING cases show higher concentrations than the MB2008 case, though the increase from the MB2008 case differs spatially between the two cases. In the BEST-FIT case, reduced scavenging amplifies the regions of elevated iron concentrations but has minimal affect on regions of low concentration; it results in larger concentration gradients that are similar to the field data (Figure 1b). In the WEAK-BINDING case, by contrast, the concentration increase is mostly seen in the regions where the concentrations are low in the MB2008 case, leading to a more homogeneous distribution. In all cases, high iron concentrations penetrate into the open ocean from the east coast of Japan at about 40°N. However, the feature is not supported by the field data where higher concentrations are rather seen further north in the subarctic region. This disagreement may be attributed to a misplaced Kuroshio current in our physical simulation, as is typical of low-resolution ocean models [e.g., *Thompson and Cheng*, 2008].

[22] In the lower pycnocline (Figures 3g–3i), the differences among the cases are similar to that shown for the upper pycnocline. The BEST-FIT case simulates well the features shown in the field data (Figure 1c): high concentrations (>0.9 nM) in the northwestern region and low concentrations (~0.7 nM) in the eastern region between 160°W and 140°W. In addition, the BEST-FIT case simulates well the high iron concentrations off the coast of California. The BEST-FIT case, however, somewhat overestimates the concentrations in the central North Pacific.

3.2. Vertical Structure

[23] In the latitudinal cross section along 165°E (Figures 4a, 4d, and 4g), only the BEST-FIT case reproduces the high iron concentration core observed by *Nishioka et al.* [2007] (Figure 4j). The structure is in good agreement with the field data: the core located at 48°N with the maximum concentration over 1 nM, and high concentrations (>0.7 nM) extending over the subtropical region through the mid and lower pycnocline. The simulated distribution, however, is somewhat shallow compared with the field data. The simulated depth of the maximum concentration core is about 700 m, but in the field data it is deeper than 1000 m; the simulated concentrations are overestimated in layers with potential density less than 26.6 σ_θ. The MB2008 and WEAK-BINDING cases fail to simulate the core structure and significantly underestimate the concentrations along this section.

[24] In the latitudinal cross section along 140°W, the iron concentrations in the field data are 0.5–0.8 nM in the lower pycnocline for latitudes poleward of 30°N (Figure 4k). The simulated results are 0.5–0.6 nM, 0.6–0.8 nM and 0.6–0.65 nM for the MB2008, BEST-FIT and WEAK-BINDING cases, respectively, all close to the field data. In addition to the concentration level, the BEST-FIT case simulates a local

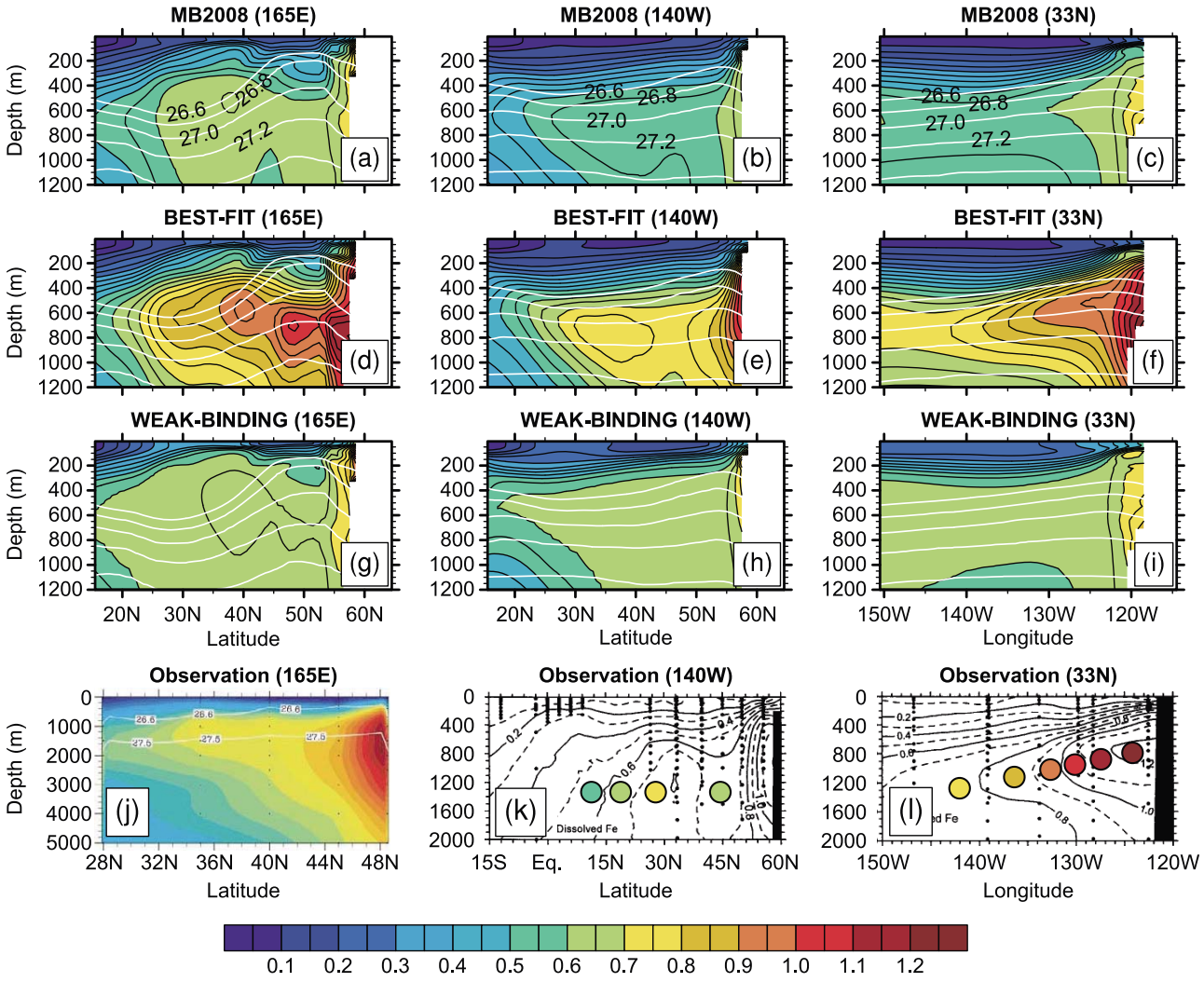

Figure 4. Latitudinal and longitudinal cross sections of the simulated dissolved iron concentrations (nM): for the MB2008 case along (a) 165°E, (b) 140°W and (c) 33°N; for the BEST-FIT case along (d) 165°E, (e) 140°W and (f) 33°N; for the WEAK-BINDING case along (g) 165°E, (h) 140°W and (i) 33°N, respectively. Observed dissolved iron concentrations along (j) 165°E [after *Nishioka et al.*, 2007], (k) 140°W and (l) 33°N [after *Johnson et al.*, 1997], respectively. Note that the vertical axes are different between the simulated results and the observed data. White lines in the simulated results are the simulated isopleths of potential density for 26.6, 26.8, 27.0, 27.2 and 27.4 σ_θ, respectively.

maximum in the subtropical region, as observed in the field data.

[25] The BEST-FIT case also reproduces a westward penetration of high concentration in the zonal section along 33°N (Figures 4f and 4l). The high concentrations over 0.7 nM extend westward beyond 140°W; this extension causes the local maximum in the simulated cross section of 140°W (Figure 4e). Such a penetration is not simulated in the MB2008 and WEAK-BINDING cases (Figures 4c and 4i).

3.3. Model-Data Comparison Scatterplots

[26] Better model skill in the BEST-FIT case is also confirmed by scatterplots of dissolved iron concentration between the field data and simulated results (Figure 5). The BEST-FIT case successfully reproduces the large range in concentration in the North Pacific and shows the highest R-squared (R^2 = 0.61) and lowest root mean square error (RMSE = 0.21 nM) among the cases. The model overestimates data in the central North Pacific (the dotted rectangular region in Figure 1). If we exclude that region (excluding 25% of the data points), then the R-squared values increase in all cases (Figures 5a–5c); the BEST-FIT case again shows the highest skill among the cases (R^2 = 0.74 and RMSE = 0.16 nM). Both the MB2008 and WEAK-BINDING cases especially fail to compute high concentrations over 0.6 nM (Figures 5d and 5f). The BEST-FIT case shows R-squared values over two times higher and RMSEs two times lower in the high concentration zone (Figure 5e), leading to the highest skill among the cases.

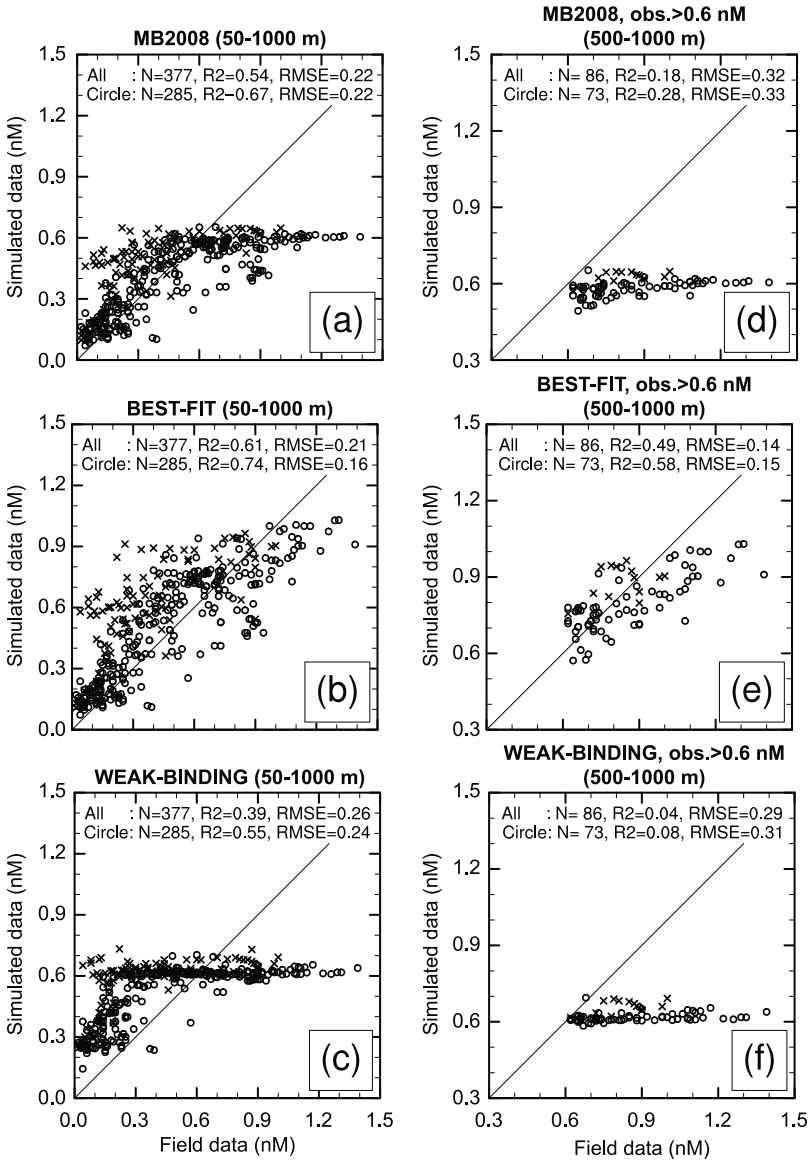

Figure 5. Scatterplots for relationship between the field data (compiled by *Moore and Braucher* [2008]; horizontal axis) and the simulated results (vertical axis) in depths between 50 and 1000 m for the (a) MB2008, (b) BEST-FIT and (c) WEAK-BINDING cases, respectively. (d-f) The same plots in depths between 500 and 1000 m and for the field data exceeding 0.6 nM. The simulated results are subsampled from the same month, location and depth as the field data. Data within 500 km of the coast are eliminated. Crosses indicate data from the central North Pacific (a region enclosed by dotted line in Figure 1); circles indicate data from the other region. "N," "R2" and "RMSE" represent the number of data, R-squared and root mean squared error, respectively. "All" and "Circle" represent the statistics for all data and only for data represented by circles in each panel, respectively.

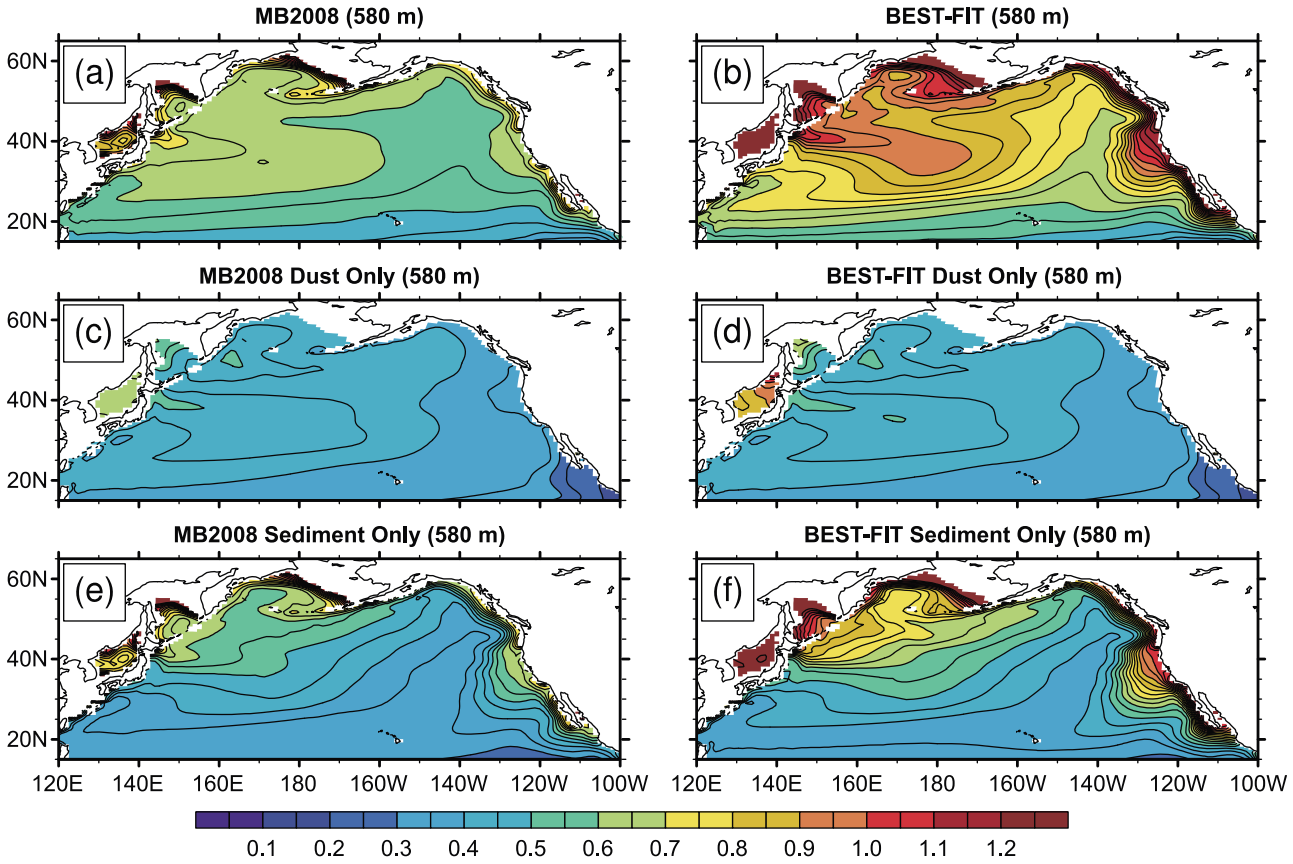

Figure 6. Horizontal distribution of simulated dissolved iron concentration (nM) at 580 m depth for the (a) MB2008, (b) BEST-FIT, (c) MB2008 Dust Only, (d) BEST-FIT Dust Only, (e) MB2008 Sediment Only and (f) BEST-FIT Sediment Only cases, respectively.

3.4. Result of Experiment Changing External Iron Sources

[27] The simulated iron distributions at midpycnocline depth in the Dust Only cases (Figures 6c and 6d) are almost the same between the MB2008 and BEST-FIT cases. By contrast, the iron distributions in the Sediment Only cases (Figures 6e and 6f) are significantly different: the concentrations increase especially in the northwestern region and off the coast of California. The results indicate that the higher ligand concentration specified in the BEST-FIT case increases sedimentary iron transport to these regions; it accounts for the better model skill in the BEST-FIT case.

4. Discussion

4.1. Scavenging Regime in the North Pacific

[28] To examine differences across model cases, we introduce the concept of an iron scavenging timescale (S_{time}) defined as

$$S_{time} \equiv -\frac{dFe}{scav} \tag{5}$$

where dFe is dissolved iron concentration and $scav$ is dFe tendency owing to iron scavenging (see equation (1)). S_{time} corresponds to the residence time of dissolved iron when we assume scavenging is the sole iron removal process. Since $scav$ is a function of sinking particle fluxes (equation (4)), the $scav$ values vary spatiotemporally. For simplicity, we assume typical sinking particle fluxes through the pycnocline of the North Pacific, the annual mean fluxes averaged over the North Pacific at 500 m depth. The S_{time} values in the MB2008 case are roughly 5 years at low iron concentrations, dropping sharply where iron concentrations exceed the prescribed ligand concentration of 0.6 nM (Figure 7a). In the BEST-FIT case, the increase in the ligand concentration pushes the threshold in S_{time} to higher concentration levels, which explains the reason why the increase in ligand concentration increases sedimentary iron transport away from the coast. The sedimentary iron flux is large around continental margins (Figure 2b), forming high local concentrations (Figures 6e and 6f) that quickly decrease offshore to below 0.6 nM in the MB2008 case owing to the short S_{time} at elevated dFe. The elongation of the S_{time} curve in the BEST-FIT case enables sedimentary iron to penetrate into the open ocean with higher iron concentrations (Figures 6f). For instance, the S_{time} values for a 1 nM iron concentration are roughly a half year and 5 years for the MB2008 and BEST-FIT cases, respectively. If we assume an advection velocity of 1 cm s^{-1}, then the spatial scales for an anomaly advected from the continental margin are approximately 150 km and 1500 km for the MB2008 and BEST-FIT cases, respectively; the latter is enough to spread well into the open ocean.

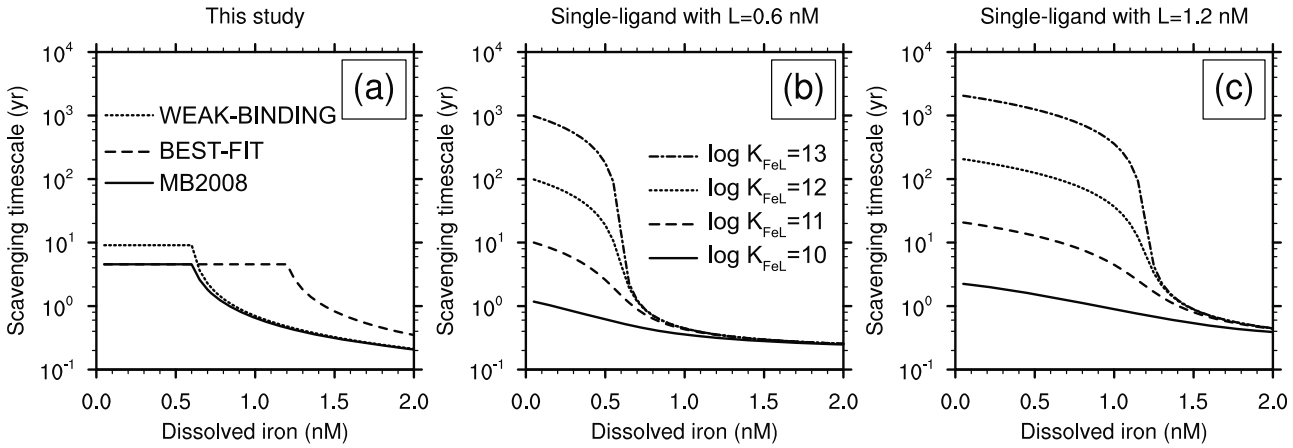

Figure 7. (a) Relationship between dissolved iron concentrations (nM) and scavenging timescale (years) for this study. Base scavenging rates (Sc_b) are assumed to be 0.22 (yr^{-1}) for the MB2008 and BEST-FIT cases and 0.11 (yr^{-1}) for the WEAK-BINDING case, respectively, the average values in the North Pacific at 500 m depth in our simulation. Solid, dashed and dotted lines indicate the MB2008, BEST-FIT and WEAK-BINDING cases, respectively. The relationship for the single-ligand model [*Archer and Johnson*, 2000] for ligand concentrations of (b) 0.6 nM and (c) 1.2 nM, respectively. Solid, dashed, dotted and chain lines indicate log K_{FeL} of 10, 11, 12 and 13, respectively. Scavenging rate for free iron (Sc') is specified at 5.6 (yr^{-1}) based on *Doney et al.* [2006].

[29] In the North Pacific, the local iron supply from aeolian dust is less intense and more spatially homogeneous (Figure 2a); thus, iron from aeolian dust rarely forms iron concentrations exceeding 0.6 nM in the open ocean in the model (Figures 6c and 6d). Therefore, the increase in S_{time} in the BEST-FIT case has minimal effects on the iron distribution supplied from aeolian dust.

[30] Our results suggest that the penetration of high iron concentrations in the northwestern Pacific and off the coast of California cannot be accounted for by an aeolian iron source alone (Figures 6c and 6d) and is evidence of the penetration of sedimentary iron into the open ocean in these areas. The penetration appears only under a scavenging regime where high iron concentrations have relatively long S_{time}, namely, on the order of years. The reason for the long S_{time} for high iron concentrations is still open to debate; but, the most plausible explanation for the longer S_{time} is higher ligand concentration.

[31] The model response in the WEAK-BINDING case is also accounted for by consideration of S_{time} (Figure 7a). S_{time} in the WEAK-BINDING case is nearly identical to that from the MB2008 case for iron concentrations exceeding the prescribed ligand concentration of 0.6 nM, but S_{time} increases to approximately 10 years for iron concentrations below the ligand concentration. The short S_{time} in the high iron concentration range prevents the offshore penetration of sedimentary iron with high concentrations. The long S_{time} in the low iron concentration range increases the low concentrations toward 0.6 nM and results in the more homogeneous subsurface distribution in the WEAK-BINDING case. The field data indicate large spatial variability even for iron levels below 0.6 nM (Figure 1); the large spatial variability at low iron concentrations indicates short S_{time} and a moderate scavenging even for iron concentrations below the binding ligand concentration. Such a moderate scavenging regime has been previously indicated in considerations of the global iron distribution [*Moore and Braucher*, 2008]; we confirm that the regime is also suitable for explaining the basin scale iron distribution in the North Pacific.

[32] A number of other models use a different, but related, scavenging parameterization based on a "single-ligand" approach [*Archer and Johnson*, 2000; *Parekh et al.*, 2005; *Doney et al.*, 2006; *Aumont and Bopp*, 2006]. Here, we consider results when we use the "single-ligand" parameterization. In this parameterization, the dissolved iron tendency owing to scavenging is

$$scav = -Sc' \times dFe' \tag{6}$$

where dFe' is the concentration of dissolved iron that is not complexed with the binding ligands (so-called free dissolved iron) and Sc' is a scavenging rate for dFe'. Note that Sc' is different from Sc used in our parameterization. Both Sc and Sc' are scavenging rates, but the former is for total dissolved iron and the latter is for free dissolved iron. If we know a total ligand concentration (L) and a conditional stability constant (K_{FeL}), we can obtain dFe' concentrations for given dFe concentrations as the positive root of a quadratic equation:

$$dFe'^2 + \left(L + \frac{1}{K} - dFe\right)dFe' - \frac{dFe}{K} = 0; \tag{7}$$

We refer to the solution of equation (7) as $dFe' = X(dFe)$. We use a parameterization for Sc' as in the work of *Doney et al.* [2006] where Sc' is simply defined as a function of depth:

$$Sc' = C_0\left\{1 + \alpha \exp\left(-\frac{z}{z_{scav}}\right)\right\} \tag{8}$$

where $C_0 = 0.2\ yr^{-1}$, $\alpha = 200$, and $z_{scav} = 250$ m; we adopt the Sc' value at 500 m depth (5.6 yr^{-1}). Substituting $dFe' =$

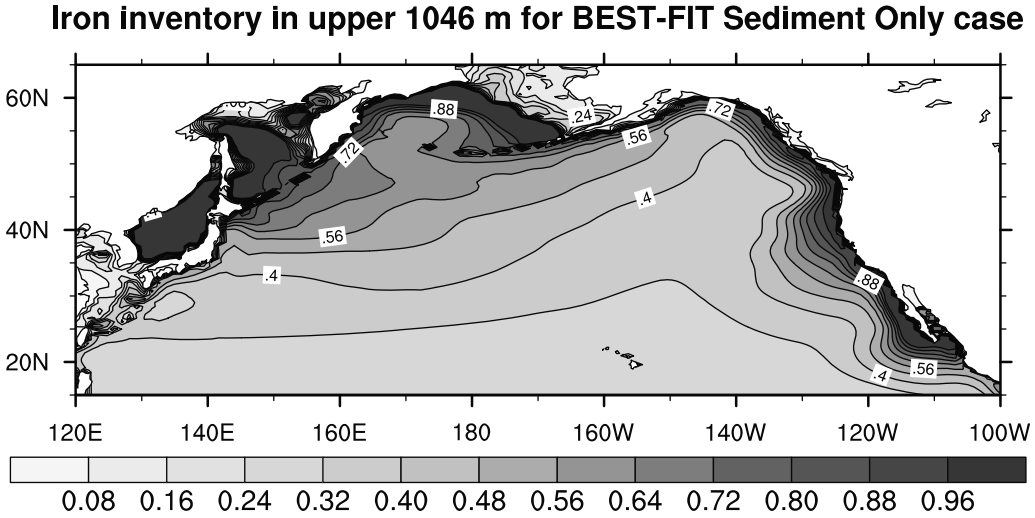

Figure 8. Horizontal distribution of the simulated dissolved iron inventory (mmol m^{-2}) in the upper 1046 m, for the BEST-FIT Sediment Only case.

$X(dFe)$ and equation (6) for equation (5), we obtain S_{time} in the single-ligand model as a function of dFe:

$$S_{time} = \frac{dFe}{Sc' \times X(dFe)}. \quad (9)$$

If we use a ligand concentration of 0.6 nM as in the MB2008 and WEAK-BINDING cases (Figure 7b), S_{time} values for high iron concentrations (~1 nM) are shorter than 1 year for any choice of K_{FeL}, so that lateral penetration of high sedimentary iron will not be simulated in this case. By contrast, a high ligand concentration of 1.2 nM results in elevated S_{time} values in the high concentration range (for moderate to large K_{FeL}) and would enable lateral penetration into the open ocean (Figure 7c). Therefore, a relatively high ligand concentration will be necessary to simulate the penetration of high iron concentrations into the basin interior.

[33] Lower stability constants will also be necessary to simulate realistic iron distributions in the North Pacific. Higher stability constants, order of log K_{FeL} = 12~13, generate long S_{time} values (>10 years) below the prescribed ligand concentrations (Figures 7b and 7c), which will result in homogeneous subsurface iron distributions as demonstrated in the WEAK-BINDING case. Therefore, the combination of a high ligand concentration and low to moderate stability constant is necessary for the simulated iron distribution in the North Pacific to be consistent with observations. This constraint is consistent with the suggestion by *Parekh et al.* [2005], though they indicated that the combination is required to account for the interocean scale iron distribution. Our results extend their suggestion for basin scale iron distribution in the North Pacific. In addition, we also find that considering sedimentary iron sources is essential to simulate iron distribution in the North Pacific.

[34] Previous electrochemical measurements suggest the presence of two classes of iron binding ligands, a strong binding ligand class (L_1) and a weaker ligand class (L_2); the L_2 class dominates in the subsurface ocean [*Rue and Bruland*, 1995; *Cullen et al.*, 2006; *Hunter and Boyd*, 2007; *Vraspir and Butler*, 2009]. *Rue and Bruland* [1995] reported high L_2 ligand concentrations (>1.5 nM) in the subsurface Pacific with low conditional stability constants (log K_{FeL} ~ 11), which are consistent with our results. However, these ligands have not been fully identified; chemical structures and the sources and sinks are still uncertain. Further investigations are required for understanding how iron-binding ligands control both intra-ocean and interocean scale iron distribution.

4.2. Process of Sedimentary Iron Transport to the Open Ocean

[35] We examine the lateral transport of sedimentary iron from the simulated iron inventory (Figure 8) and tendency terms (Figure 9) for the BEST-FIT Sediment Only case. The prognostic equation for dissolved iron concentration is written as

$$\frac{\partial dFe}{\partial t} = ADV + MIX + BGC + FRC, \quad (10)$$

where ADV represents iron flux convergence owing to large-scale flow; MIX represents iron flux convergence owing to mixing processes that include effects of subgrid-scale eddies, isopycnal and diapycnal mixing; BGC represents biogeochemical processes; and FRC represents external iron forcings. We calculate each of the terms on the right hand side of equation (10), and then average them for a year and over the upper 1046 m (Figure 9). The iron distribution in the simulation is almost in steady state; thus, the left-hand term is nearly equal to zero. Since we consider the BEST-FIT Sediment Only case, FRC does not include iron from aeolian dust.

[36] Sedimentary iron is supplied around shelf regions (Figure 9d) and is eventually removed from the ocean by iron scavenging (Figure 9c). The widespread distribution of iron scavenging indicates that the physical processes transport sedimentary iron to the open ocean (Figures 9a and 9b). In the northwestern region, ADV shows large positive values (advective convergence) (Figure 9a), meaning that large-scale flow supplies sedimentary iron to the region. The fluxes come from the west, the origin in the western boundary

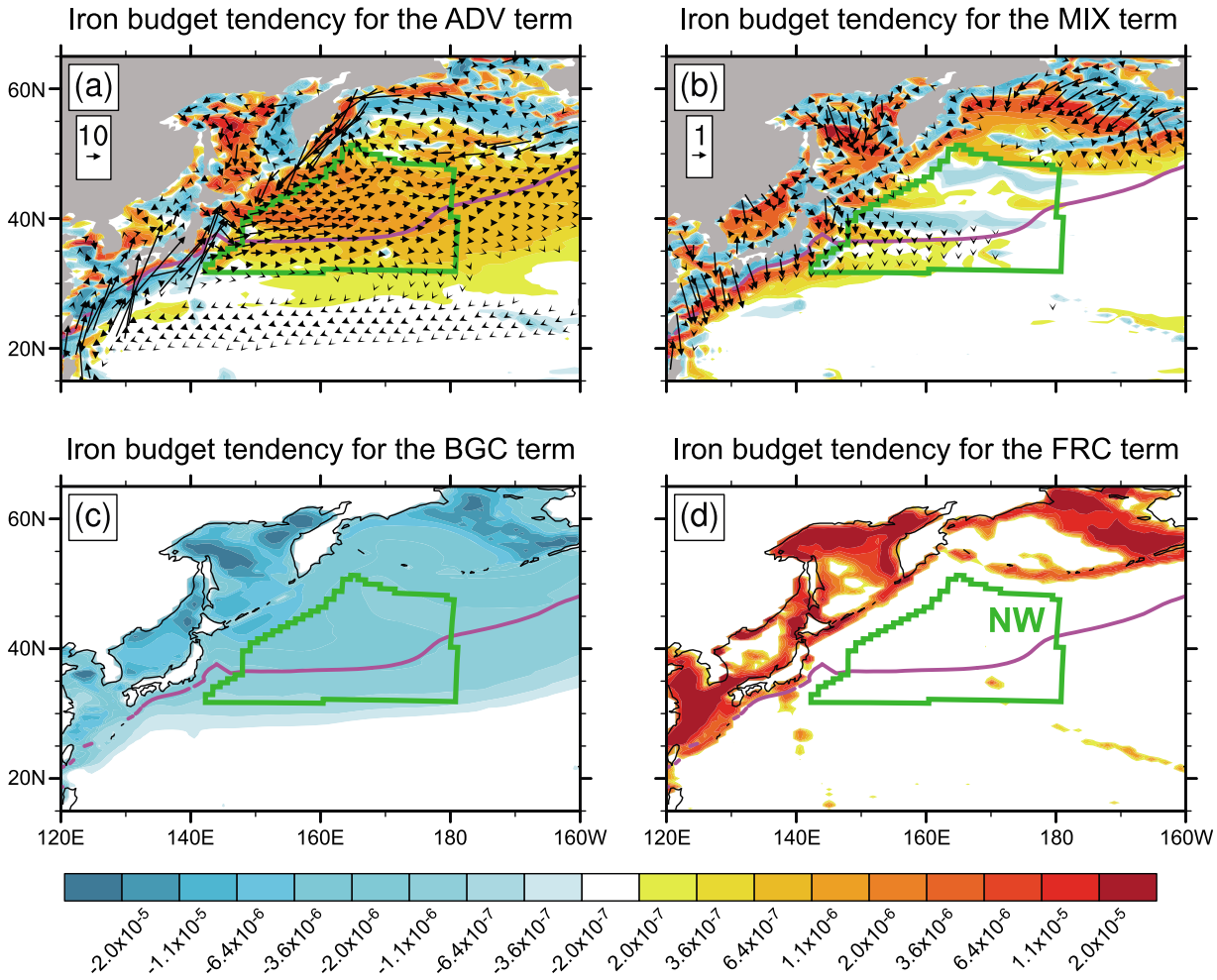

Figure 9. Annual mean dissolved iron budget tendency averaged over the upper 1046 m of the western North Pacific for the BEST-FIT Sediment Only case. Dissolved iron fluxes (vectors, units are in nmol m^{-2} s^{-1}) and their convergence (shades with positive values, units are in nmol m^{-3} s^{-1}) and divergence (shades with negative values) by (a) large-scale flow and (b) mixing processes. Note that the flux convergences and divergences are calculated for all components (including the vertical component), though the fluxes are only displayed in the horizontal components. Vectors below 2.0 nmol m^{-2} s^{-1} and 0.2 nmol m^{-2} s^{-1} are omitted for the large-scale flow and mixing processes, respectively. Dissolved iron tendency (nmol m^{-3} s^{-1}) by (c) net biogeochemical processes and (d) iron supply from seafloor sediment. A purple line indicates a contour line of iron inventory for 0.48 mmol m^{-2} (see Figure 8). A box area enclosed by green line is defined as an open ocean region of the northwestern North Pacific (NW) and is used for regional iron budget analysis (Figure 10).

currents with large iron fluxes: the Kuroshio, East Kamchatka and East Sakhalin Currents. These western boundary currents take up sedimentary iron around shelf regions, confirmed by the negative flux convergences (Figure 9a).

[37] The fluxes in *ADV* mainly diverge somewhat offshore of the shelf regions (Figure 9a), the reason being lateral iron transport by horizontal mixing (Figure 9b). The fluxes in *MIX* diverge in shelf regions and converge in offshore regions, reflecting the mixing of coastal waters with open ocean waters and transport of iron to the offshore regions. Thus, the boundary currents take iron transported by the mixing processes, in addition to direct uptake from shelf sediment; then, the currents transport it along the coasts and finally supply it to the open ocean.

[38] Comparison of iron budget tendency terms in an open ocean region of the northwestern Pacific (the NW region in Figure 9d) for the BEST-FIT Sediment Only and BEST-FIT Dust Only cases reveals the relative importance of sedimentary and aeolian iron sources in this region (Figures 10a and 10b). In the Sediment Only case, iron supply by horizontal advection (*ADVh*) dominates in the upper 1046 m and balances iron removal by *BGC* (Figure 10a). In the Dust Only case, by contrast, iron supply from aeolian source (*FRC*) mainly contributes to the iron inventory in the upper 1046 m with a minor contribution from *ADVh* (Figure 10b). Although the dominant iron supply process is different for each case, the total iron supply to the upper 1046 m of the NW region is very similar in both the cases, about 40 μmol m^{-2} yr^{-1}, indicating equal importance of aeolian and sedimentary iron

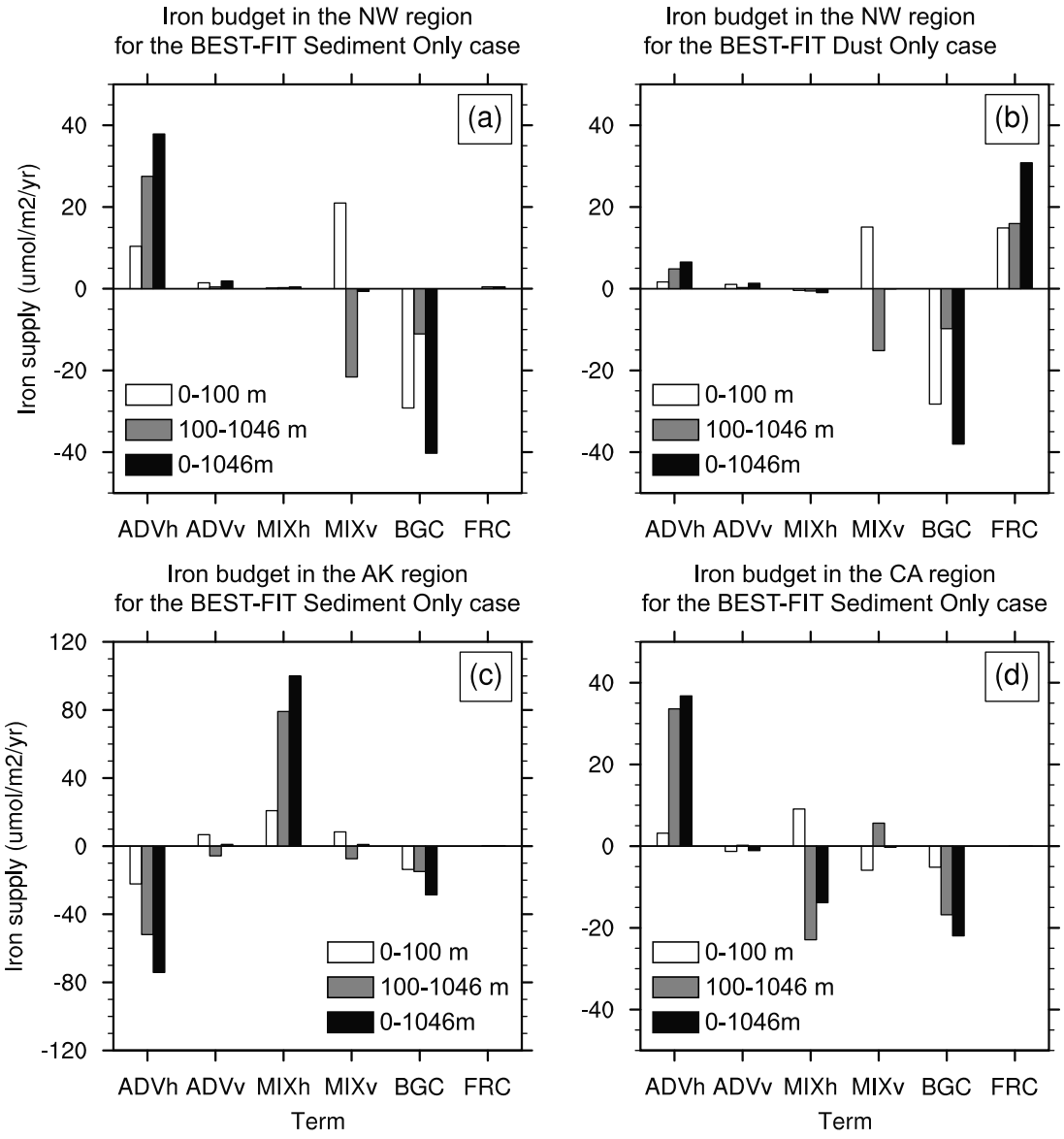

Figure 10. Annual mean dissolved iron budget (μmol m^{-2} yr^{-1}) averaged in the NW region (see Figure 9) for the (a) BEST-FIT Sediment Only and (b) BEST-FIT Dust Only cases, respectively. The same budget averaged in the (c) AK and (d) CA regions (Figure 11) for the BEST-FIT Sediment Only case, respectively. The white, gray and black bars indicate results vertically integrated over 0–100 m, 100–1046 m and 0–1046 m, respectively. ADV, MIX, BGC and FRC represent iron supply to (positive) and removal from (negative) each region owing to large-scale flow, mixings, biogeochemical processes and external iron sources, respectively. "h" and "v" in ADV and MIX mean the horizontal and vertical components, respectively.

sources in this region [see also *Moore and Braucher*, 2008]. In the full BEST-FIT case, including both the aeolian and sedimentary sources, the total iron supply to the upper 1046 m of the NW region is 73.2 μmol m^{-2} yr^{-1}, slightly smaller than the sum of the Dust Only and Sediment Only cases (77.6 μmol m^{-2} yr^{-1}). Higher iron concentrations in the full BEST-FIT case make for stronger iron scavenging, resulting in a lower iron input into the NW region. It is, however, a minor effect on the result (less than 10%).

[39] The same is true for surface iron inventory; total iron supply to the upper 100 m is the same level, approximately 30 μmol m^{-2} yr^{-1}, for both the cases (Figures 10a and 10b). Note that, in the Dust Only case, direct aeolian iron supply to the surface (*FRC*) explains only a half of the whole surface iron supply owing to aeolian source. Iron dissolved from dust particles in subsurface water and iron recycled in the ocean interior are supplied to the surface by vertical mixing (*MIXv*), which explains the other half of surface iron supply in the Dust Only case. In the Sediment Only case, the term balance for the 100–1046 m depth band shows a large iron supply by *ADVh* and removal by *MIXv* (Figure 10a), indicating horizontal transport of sedimentary iron to the NW region through the subsurface followed by iron supply to the surface by vertical mixing.

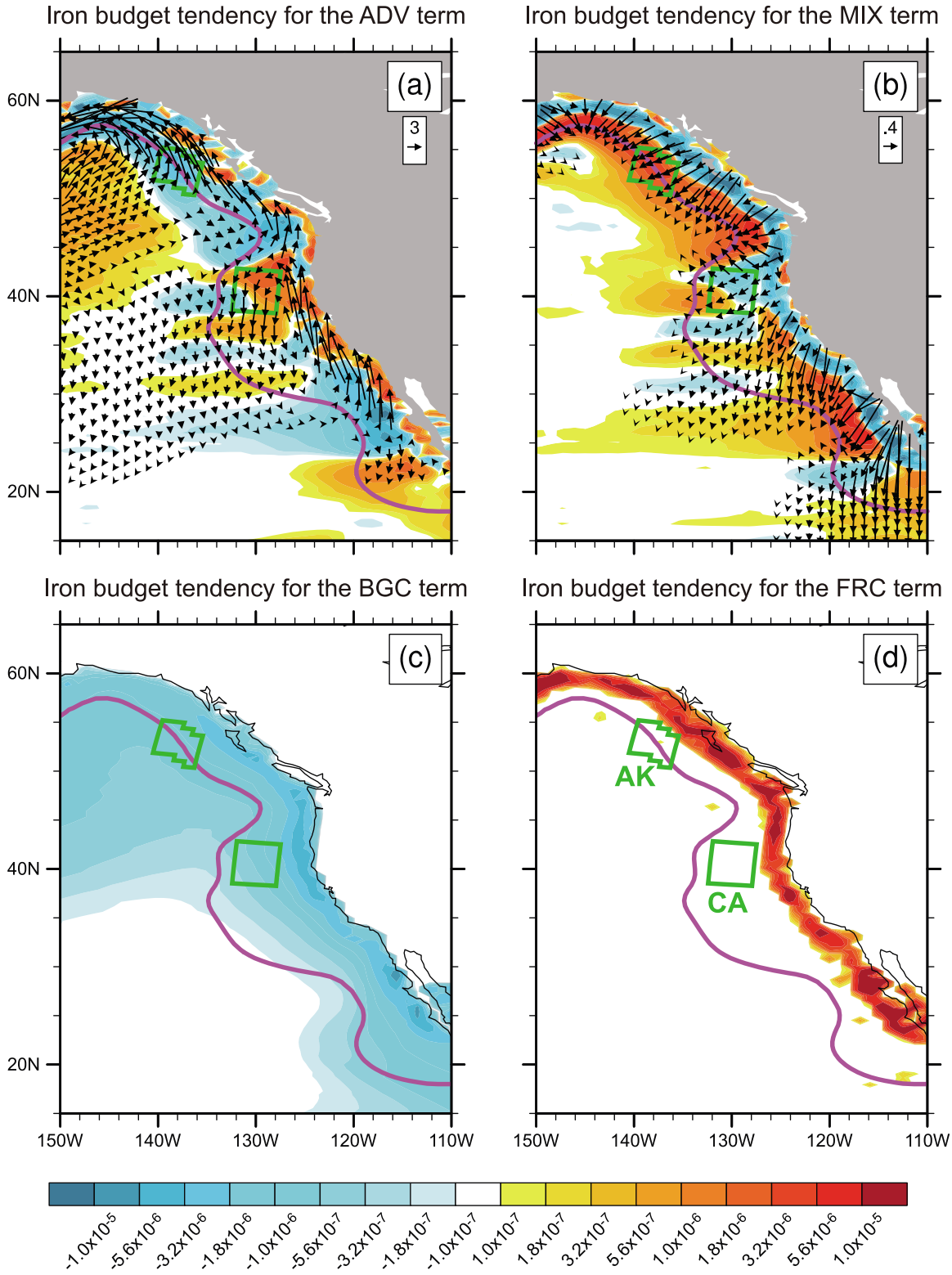

Figure 11. The same as Figure 9, but for the eastern North Pacific. Vectors below 1.0 nmol m^{-2} s^{-1} and 0.1 nmol m^{-2} s^{-1} are omitted for the large-scale flow and mixing processes, respectively. Box areas enclosed by green line are defined as regions of off the coast of California (CA) and Alaska (AK), respectively, and are used for regional iron budget analysis (Figure 10).

[40] *Nishioka et al.* [2007] have suggested that sedimentary iron is an essential iron source and contributes to surface biological production in the northwestern North Pacific. Our results are consistent with their suggestion; the sedimentary source contributes to the iron inventory both in the surface and upper 1000 m with the same magnitude as aeolian source. However, further investigation is needed, especially for iron supply to the surface, because our result will overestimate the contribution of *MIXv* owing to the shallower simulated vertical structure (Figure 4b). *Nishioka et al.* [2007] attributed the origin of sedimentary iron in the northwestern region to the shelf region of the Okhotsk Sea. Since our model does not fully resolve the Okhotsk Sea, it is difficult to discuss the role of the Okhotsk Sea. However, our results indicate that the northwestern North Pacific receives sedimentary iron from various regions besides the Okhotsk Sea through the western boundary currents. Possible origins of sedimentary iron distributed in the northwestern region include the shelf regions of Kuril Islands, Kamchatka Peninsula, Bering Sea and Japanese Archipelago (Figure 9a).

[41] Our iron budget for the eastern North Pacific reveals that the separation of currents from the coast is important for determining the sedimentary iron distribution off the coast of California (Figure 11). Offshore iron transport by horizontal mixing is broadly seen along the west coast of the North American continent (Figure 11b); the diffusive transport supports the divergence in the advection fluxes toward the coast (Figure 11a). The contribution of diffusive mixing *MIXh* to advective divergence *ADVh* is confirmed in the iron budget averaged over the AK region (Figure 10c), a typical offshore region in the eastern subarctic (Figure 11d). A large part, about 75% for the 0–1046 m range, of iron supplied to the AK region by mixing from the inshore sediment source is subsequently exported by advection to the northwest following the boundary current flow, with local biogeochemical processes removing only 25%. This is a typical term balance in offshore regions of the west coast of the North American continent; sedimentary iron does not extend much offshore in regions under such a term balance.

[42] The situation is different off the coast of California. Advection fluxes along the coast turn offshore around 42°N; convergence of the offshore fluxes expands the region of influence (Figure 11a). The subsurface term balance for the CA region confirms horizontal advection as the main contribution to iron export to this region (Figure 10d, the 100–1046 m range). In addition, a large part of the offshore exported iron results in the flux divergence in horizontal mixing (Figures 10d and 11b), indicating that the advective iron export causes a large local concentration gradient and further offshore iron transport by horizontal mixing. A separation from the coast of the alongshore currents around 42°N is known from the field data [*Barth et al.*, 2000]; thus the separation likely triggers offshore sedimentary iron transport off the coast of California.

5. Conclusion

[43] We have examined the mechanisms controlling dissolved iron distributions in the North Pacific using the Biogeochemical Elemental Cycling model configured at a medium spatial resolution. The simulation reproduces well the main features in the iron distribution of the North Pacific: iron concentrations are especially high in the northwestern region and off the coast of California with large horizontal concentration gradients below the surface. Experiments with different iron scavenging parameter values reveal a plausible iron scavenging regime in the North Pacific: high iron concentrations (~1 nM) have long residence times of the order of years, and iron concentrations below the binding ligand concentration are subject to a moderate scavenging. The experiments with either aeolian or sedimentary iron sources alone demonstrate that lateral transport of sedimentary iron to the open ocean causes the high iron concentrations in the northwestern North Pacific and off the coast of California. Detailed transport processes differ in each region, but some major processes are similar. The subsurface currents pick up sedimentary iron by mixing coastal and open ocean waters; then, currents transport iron along the coasts with continuous uptake of sedimentary iron from the shelf regions. In the regions where the alongshore currents leave the coasts, sedimentary iron is transported offshore into the open ocean. The existence of offshore directed currents is essential for the lateral penetration of sedimentary iron to the open ocean. This horizontal transport of sedimentary iron into the ocean interior plays a crucial role and characterizes the dissolved iron distribution in the North Pacific.

Appendix A: Comparison of Iron Scavenging in Different Formulations

[44] Here we compare intensity of iron scavenging ($|scav|$) in our model (equations (1)–(4)) and in the single-ligand model (equations (6)–(8)). We assume typical scavenging rates at 500 m depth for total dissolved iron (Sc_b = 0.22 yr^{-1} for the MB2008 and BEST-FIT cases; Sc_b = 0.11 yr^{-1} for the WEAK-BINDING case, respectively) and for free dissolved iron (Sc' = 5.6 yr^{-1}) as described in the discussion section, and use the same scavenging parameters as used in Figure 7. For both the formulations, we calculate the $|scav|$ values as a function of total dissolved iron (dFe); thus, the $|scav|$ term in the single ligand model is $Sc' \times X(dFe)$, and X is the positive root of equation (7). The $|scav|$ values are similar to each other for the cases with the same total ligand concentration (L) (Figure A1): the MB2008 and WEAK-BINDING cases in Figure A1a and all cases in Figure A1b (L = 0.6 nM); the BEST-FIT case in Figure A1a and all cases in Figure A1c (L = 1.2 nM), meaning that experiments using the different formulations with the same total ligand concentration result in similar dissolved iron distributions.

[45] We note that our iron scavenging formulation has a second order dependence on dFe at high iron concentration levels (equations (1) and (3); Figure A1a), which is different from the linear relationship usually assumed for oceanic elemental scavenging [*Craig*, 1974; *Clegg et al.*, 1991; *Johnson et al.*, 1997; *Archer and Johnson*, 2000; *Parekh et al.*, 2004]. However, over the observed range of dFe, the functional shape of $|scav|$ in our model is similar to that in the single-ligand model with lower conditional stability constants ($\log K_{FeL}$ = 10~11) that are considered adequate for simulating global iron distribution [*Parekh et al.*, 2004], indicating reasonableness of our formulation.

[46] The $|scav|$ values in the single ligand model show nonlinear behavior for dFe especially for cases with lower

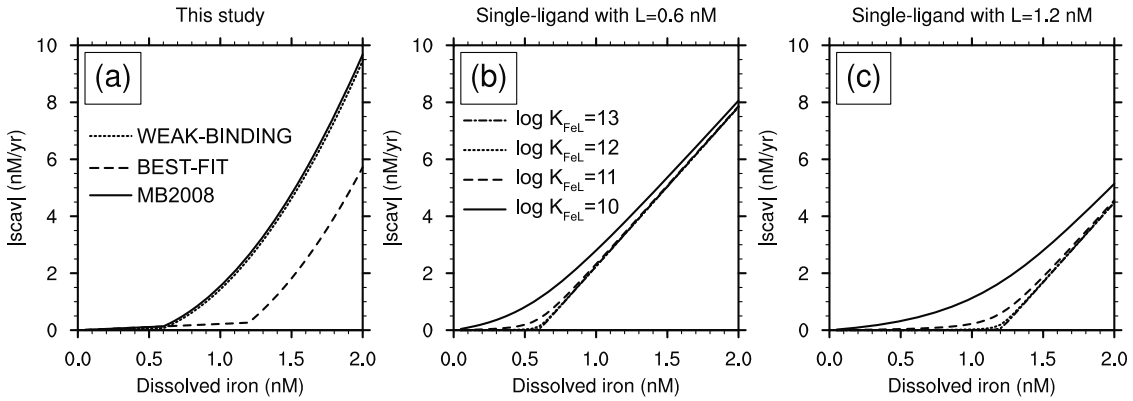

Figure A1. (a) Relationship between total dissolved iron concentrations (nM) and scavenging intensity (nM yr^{-1}) for this study. Base scavenging rates (Sc_b) are assumed to be 0.22 (yr^{-1}) for the MB2008 and BEST-FIT cases and 0.11 (yr^{-1}) for the WEAK-BINDING case, respectively, the average value in the North Pacific at 500 m depth in our simulation. Solid, dashed and dotted lines indicate the MB2008, BEST-FIT and WEAK-BINDING cases, respectively. The same relationship for the single-ligand model [*Archer and Johnson*, 2000] for ligand concentrations of (b) 0.6 nM and (c) 1.2 nM, respectively. Solid, dashed, dotted and chain lines indicate log K_{FeL} of 10, 11, 12 and 13, respectively. Scavenging rate for free iron (Sc') is specified at 5.6 (yr^{-1}) based on *Doney et al.* [2006].

stability constants (log K_{FeL} = 10~11) near the prescribed ligand concentrations (0.6 and 1.2 nM for Figures A1b and A1c, respectively), even though the model assumes a linear scavenging relationship for dFe' (equation (6)). The nonlinearity arises from the nonlinear increase in the fraction of dFe' to dFe (the positive root of equation (7)), and lower stability constants (weak binding) cause a higher dFe' fraction, resulting in more obvious nonlinear behavior.

[47] We note that such nonlinear behavior in the single ligand model differs from the second-order behavior in our formulation in that the single ligand model approaches linearity for high iron concentration levels. Assuming a total dissolved iron concentration much higher than a total ligand concentration ($dFe \sim dFe - L$), the positive root of equation (7) yields a relationship where $dFe' \sim dFe$; thus the $|scav|$ curves in the single ligand model asymptote toward a line of $Sc' \times dFe$ (Figures A1b and A1c) and do not show nonlinear behavior in high iron concentration levels.

[48] We also note that our formulation does not explicitly include values for the conditional stability constant (K), though the value is implicitly included in parameters of Sc_b and C_{high}. We discuss effect of different stability constants on simulated dissolved iron distributions by comparing functional shapes in our formulation with those in the single-ligand model (see section 4 and Figure 7).

[49] **Acknowledgments.** The authors would like to thank T. Yoshimura and K. I. Ohshima for discussion and giving comments. This work was supported by the U.S. National Science Foundation (EF-0424599). The National Center for Atmospheric Research is sponsored by the National Science Foundation.

References

Archer, D. E., and K. Johnson (2000), A model of the iron cycle in the ocean, *Global Biogeochem. Cycles*, *14*(1), 269–279, doi:10.1029/1999GB900053.

Aumont, O., and L. Bopp (2006), Globalizing results from ocean in situ iron fertilization studies, *Global Biogeochem. Cycles*, *20*, GB2017, doi:10.1029/2005GB002591.

Barbeau, K. (2006), Photochemistry of organic iron(III) complexing ligands in oceanic systems, *Photochem. Photobiol.*, *82*(6), 1505–1516.

Barth, J. A., S. D. Pierce, and R. L. Smith (2000), A separating coastal upwelling jet at Cape Blanco, Oregon and its connection to the California Current System, *Deep Sea Res., Part II*, *47*(5–6), 783–810, doi:10.1016/S0967-0645(99)00127-7.

Berman-Frank, I., J. T. Cullen, Y. Shaked, R. M. Sherrell, and P. G. Falkowski (2001), Iron availability, cellular iron quotas, and nitrogen fixation in Trichodesmium, *Limnol. Oceanogr.*, *46*(6), 1249–1260, doi:10.4319/lo.2001.46.6.1249.

Boyle, E. (1997), What controls dissolved iron concentrations in the world ocean?—A comment, *Mar. Chem.*, *57*(3–4), 163–167, doi:10.1016/S0304-4203(97)00044-3.

Clegg, S. L., M. P. Bacon, and M. Whitfield (1991), Application of a generalized scavenging model to thorium isotope and particle data at equatorial and high-latitude sites in the Pacific-Ocean, *J. Geophys. Res.*, *96*(C11), 20,655–20,670, doi:10.1029/91JC01784.

Collins, W. D., et al. (2006), The Community Climate System Model version 3(CCSM3), *J. Clim.*, *19*(11), 2122–2143, doi:10.1175/JCLI3761.1.

Conkright, M. E., et al. (1998), World Ocean Atlas Database 1998 CD-ROM data set documentation, report, Natl. Oceanogr. Data Cent., Natl. Oceanic and Atmos. Admin., Silver Spring, Md.

Craig, H. (1974), Scavenging model for trace-elements in deep-sea, *Earth Planet. Sci. Lett.*, *23*(1), 149–159, doi:10.1016/0012-821X(74)90042-9.

Cullen, J. T., B. A. Bergquist, and J. W. Moffett (2006), Thermodynamic characterization of the partitioning of iron between soluble and colloidal species in the Atlantic Ocean, *Mar. Chem.*, *98*(2–4), 295–303, doi:10.1016/j.marchem.2005.10.007.

Danabasoglu, G., W. G. Large, J. J. Tribbia, P. R. Gent, B. P. Briegleb, and J. C. McWilliams (2006), Diurnal coupling in the tropical oceans of CCSM3, *J. Clim.*, *19*(11), 2347–2365, doi:10.1175/JCLI3739.1.

de Baar, H. J. W., and J. T. M. de Jong (2001), Distributions, sources and sinks of iron in seawater, in *Biogeochemistry of Iron in Seawater*, John Wiley, Hoboken, N. J.

Doney, S. C., K. Lindsay, I. Fung, and J. John (2006), Natural variability in a stable, 1000-yr global coupled climate-carbon cycle simulation, *J. Clim.*, *19*(13), 3033–3054, doi:10.1175/JCLI3783.1.

Doney, S. C., I. Lima, R. A. Feely, D. M. Glover, K. Lindsay, N. Mahowald, J. K. Moore, and R. Wanninkhof (2009a), Mechanisms governing interannual variability in upper-ocean inorganic carbon system and air-sea CO_2 fluxes: Physical climate and atmospheric dust, *Deep Sea Res., Part II*, *56*(8–10), 640–655, doi:10.1016/j.dsr2.2008.12.006.

Doney, S. C., I. Lima, J. K. Moore, K. Lindsay, M. J. Behrenfeld, T. K. Westberry, N. Mahowald, D. M. Glover, and T. Takahashi (2009b), Skill metrics for confronting global upper ocean ecosystem-biogeochemistry models against field and remote sensing data, *J. Mar. Syst.*, *76*(1–2), 95–112, doi:10.1016/j.jmarsys.2008.05.015.

Duce, R. A., and N. W. Tindale (1991), Atmospheric transport of iron and its deposition in the ocean, *Limnol. Oceanogr.*, *36*(8), 1715–1726, doi:10.4319/lo.1991.36.8.1715.

Elrod, V. A., W. M. Berelson, K. H. Coale, and K. S. Johnson (2004), The flux of iron from continental shelf sediments: A missing source for global budgets, *Geophys. Res. Lett.*, *31*, L12307, doi:10.1029/2004GL020216.

Falkowski, P. G. (1997), Evolution of the nitrogen cycle and its influence on the biological sequestration of CO_2 in the ocean, *Nature*, *387*(6630), 272–275, doi:10.1038/387272a0.

Falkowski, P. G., R. T. Barber, and V. Smetacek (1998), Biogeochemical controls and feedbacks on ocean primary production, *Science*, *281*(5374), 200–206, doi:10.1126/science.281.5374.200.

Fung, I. Y., S. K. Meyn, I. Tegen, S. C. Doney, J. G. John, and J. K. B. Bishop (2000), Iron supply and demand in the upper ocean, *Global Biogeochem. Cycles*, *14*(1), 281–295, doi:10.1029/1999GB900059.

Gregg, W. W., P. Ginoux, P. S. Schopf, and N. W. Casey (2003), Phytoplankton and iron: Validation of a global three-dimensional ocean biogeochemical model, *Deep Sea Res., Part II*, *50*(22–26), 3143–3169.

Huffman, G. J., R. F. Adler, P. Arkin, A. Chang, R. Ferraro, A. Gruber, J. Janowiak, A. McNab, B. Rudolf, and U. Schneider (1997), The Global Precipitation Climatology Project (GPCP) combined precipitation dataset, *Bull. Am. Meteorol. Soc.*, *78*(1), 5–20, doi:10.1175/1520-0477(1997)078<0005:TGPCPG>2.0.CO;2.

Hunter, K. A., and P. W. Boyd (2007), Iron-binding ligands and their role in the ocean biogeochemistry of iron, *Environ. Chem.*, *4*, 221–232, doi:10.1071/EN07012.

Johnson, K. S., R. M. Gordon, and K. H. Coale (1997), What controls dissolved iron concentrations in the world ocean?, *Mar. Chem.*, *57*(3–4), 137–161, doi:10.1016/S0304-4203(97)00043-1.

Kalnay, E., et al. (1996), The NCEP/NCAR 40-year reanalysis project, *Bull. Am. Meteorol. Soc.*, *77*(3), 437–471, doi:10.1175/1520-0477(1996)077<0437:TNYRP>2.0.CO;2.

Key, R. M., A. Kozyr, C. L. Sabine, K. Lee, R. Wanninkhof, J. L. Bullister, R. A. Feely, F. J. Millero, C. Mordy, and T. -H. Peng (2004), A global ocean carbon climatology: Results from Global Data Analysis Project (GLODAP), *Global Biogeochem. Cycles*, *18*, GB4031, doi:10.1029/2004GB002247.

Kustka, A. B., S. A. Sanudo-Wilhelmy, E. J. Carpenter, D. Capone, J. Burns, and W. G. Sunda (2003), Iron requirements for dinitrogen- and ammonium-supported growth in cultures of Trichodesmium (IMS 101): Comparison with nitrogen fixation rates and iron: Carbon ratios of field populations, *Limnol. Oceanogr.*, *48*(5), 1869–1884, doi:10.4319/lo.2003.48.5.1869.

Large, W. G., and S. G. Yeager (2004), Diurnal to decadal global forcing for ocean and sea-ice models: The data sets and flux climatologies, *NCAR Tech. Note 460*, 105 pp., Natl. Cent. for Atmos. Res., Boulder, Colo.

Lefevre, N., and A. J. Watson (1999), Modeling the geochemical cycle of iron in the oceans and its impact on atmospheric CO_2 concentrations, *Global Biogeochem. Cycles*, *13*(3), 727–736, doi:10.1029/1999GB900034.

Locarnini, R., A. Mishonov, J. Antonov, T. Boyer, and H. Garcia (2006), World ocean atlas 2005, U.S. Gov. Print. Off., Washington, D. C.

Luo, C., N. M. Mahowald, and J. del Corral (2003), Sensitivity study of meteorological parameters on mineral aerosol mobilization, transport, and distribution, *J. Geophys. Res.*, *108*(D15), 4447, doi:10.1029/2003JD003483.

Martin, J. H., and S. E. Fitzwater (1988), Iron-deficiency limits phytoplankton growth in the northeast Pacific subarctic, *Nature*, *331*(6154), 341–343, doi:10.1038/331341a0.

Martin, J. H., R. M. Gordon, and S. E. Fitzwater (1990), Iron in Antarctic waters, *Nature*, *345*(6271), 156–158, doi:10.1038/345156a0.

Martin, J. H., et al. (1994), Testing the iron hypothesis in ecosystems of the equatorial Pacific Ocean, *Nature*, *371*(6493), 123–129, doi:10.1038/371123a0.

Measures, C. I., and S. Vink (1999), Seasonal variations in the distribution of Fe and Al in the surface waters of the Arabian Sea, *Deep Sea Res., Part II*, *46*(8–9), 1597–1622, doi:10.1016/S0967-0645(99)00037-5.

Michaels, A. F., D. Olson, J. L. Sarmiento, J. W. Ammerman, K. Fanning, R. Jahnke, A. H. Knap, F. Lipschultz, and J. M. Prospero (1996), Inputs, losses and transformations of nitrogen and phosphorus in the pelagic North Atlantic Ocean, *Biogeochemistry*, *35*(1), 181–226, doi:10.1007/BF02179827.

Mills, M. M., C. Ridame, M. Davey, J. La Roche, and R. J. Geider (2004), Iron and phosphorus co-limit nitrogen fixation in the eastern tropical North Atlantic, *Nature*, *429*(6989), 292–294, doi:10.1038/nature02550.

Moore, J. K., and O. Braucher (2008), Sedimentary and mineral dust sources of dissolved iron to the world ocean, *Biogeosciences*, *5*(3), 631–656, doi:10.5194/bg-5-631-2008.

Moore, J. K., and S. C. Doney (2007), Iron availability limits the ocean nitrogen inventory stabilizing feedbacks between marine denitrification and nitrogen fixation, *Global Biogeochem. Cycles*, *21*, GB2001, doi:10.1029/2006GB002762.

Moore, J. K., S. C. Doney, and K. Lindsay (2004), Upper ocean ecosystem dynamics and iron cycling in a global three-dimensional model, *Global Biogeochem. Cycles*, *18*, GB4028, doi:10.1029/2004GB002220.

Morel, F. M. M., and N. M. Price (2003), The biogeochemical cycles of trace metals in the oceans, *Science*, *300*(5621), 944–947, doi:10.1126/science.1083545.

Nakamura, T., and T. Awaji (2004), Tidally induced diapycnal mixing in the Kuril Straits and its role in water transformation and transport: A three-dimensional nonhydrostatic model experiment, *J. Geophys. Res.*, *109*, C09S07, doi:10.1029/2003JC001850.

Nakamura, T., T. Toyoda, Y. Ishikawa, and T. Awaji (2006), Effects of tidal mixing at the Kuril Straits on North Pacific ventilation: Adjustment of the intermediate layer revealed from numerical experiments, *J. Geophys. Res.*, *111*, C04003, doi:10.1029/2005JC003142.

Nishioka, J., S. Takeda, I. Kudo, D. Tsumune, T. Yoshimura, K. Kuma, and A. Tsuda (2003), Size-fractionated iron distributions and iron-limitation processes in the subarctic NW Pacific, *Geophys. Res. Lett.*, *30*(14), 1730, doi:10.1029/2002GL016853.

Nishioka, J., et al. (2007), Iron supply to the western subarctic Pacific: Importance of iron export from the Sea of Okhotsk, *J. Geophys. Res.*, *112*, C10012, doi:10.1029/2006JC004055.

Ohshima, K. I., D. Simizu, M. Itoh, G. Mizuta, Y. Fukamachi, S. C. Riser, and M. Wakatsuchi (2004), Sverdrup balance and the cyclonic gyre in the Sea of Okhotsk, *J. Phys. Oceanogr.*, *34*(2), 513–525, doi:10.1175/1520-0485(2004)034<0513:SBATCG>2.0.CO;2.

Parekh, P., M. J. Follows, and E. Boyle (2004), Modeling the global ocean iron cycle, *Global Biogeochem. Cycles*, *18*, GB1002, doi:10.1029/2003GB002061.

Parekh, P., M. J. Follows, and E. A. Boyle (2005), Decoupling of iron and phosphate in the global ocean, *Global Biogeochem. Cycles*, *19*, GB2020, doi:10.1029/2004GB002280.

Parekh, P., F. Joos, and S. A. Muller (2008), A modeling assessment of the interplay between aeolian iron fluxes and iron-binding ligands in controlling carbon dioxide fluctuations during Antarctic warm events, *Paleoceanography*, *23*, PA4202, doi:10.1029/2007PA001531.

Rue, E. L., and K. W. Bruland (1995), Complexation of iron(Iii) by natural organic-ligands in the central North Pacific as determined by a new competitive ligand equilibration adsorptive cathodic stripping voltammetric method, *Mar. Chem.*, *50*(1–4), 117–138, doi:10.1016/0304-4203(95)00031-L.

Shcherbina, A. Y., L. D. Talley, and D. L. Rudnick (2003), Direct observations of North Pacific ventilation: Brine rejection in the Okhotsk Sea, *Science*, *302*(5652), 1952–1955, doi:10.1126/science.1088692.

Smith, R. D., and P. R. Gent (2004), Reference manual for the Parallel Ocean Program (POP), ocean component of the Community Climate System Model (CCSM2.0 and 3.0), *Tech. Rep. LA-UR-02–2484*, 75 pp., Los Alamos National Lab., Los Alamos, N. M.

Steele, M., R. Morley, and W. Ermold (2001), PHC: A global ocean hydrography with a high-quality Arctic Ocean, *J. Clim.*, *14*(9), 2079–2087, doi:10.1175/1520-0442(2001)014<2079:PAGOHW>2.0.CO;2.

Tagliabue, A., et al. (2010), Hydrothermal contribution to the oceanic dissolved iron inventory, *Nat. Geosci.*, *3*(4), 252–256, doi:10.1038/ngeo818.

Takata, H., K. Kuma, Y. Saitoh, M. Chikira, S. Saitoh, Y. Isoda, S. Takagi, and K. Sakaoka (2006), Comparing the vertical distribution of iron in the eastern and western North Pacific Ocean, *Geophys. Res. Lett.*, *33*, L02613, doi:10.1029/2005GL024538.

Thompson, L., and W. Cheng (2008), Water masses in the Pacific in CCSM3, *J. Clim.*, *21*(17), 4514–4528, doi:10.1175/2008JCLI2280.1.

Uchimoto, K., T. Nakamura, J. Nishioka, H. Mitsudera, M. Yamamoto-Kawai, K. Misumi, and D. Tsumune (2011), Simulations of chlorofluorocarbons in and around the Sea of Okhotsk: Effects of tidal mixing and brine rejection on the ventilation, *J. Geophys. Res.*, *116*, C02034, doi:10.1029/2010JC006487.

Vink, S., and C. I. Measures (2001), The role of dust deposition in determining surface water distributions of Al and Fe in the South West Atlantic, *Deep Sea Res., Part II*, *48*(13), 2787–2809, doi:10.1016/S0967-0645(01)00018-2.

Vraspir, J. M., and A. Butler (2009), Chemistry of marine ligands and siderophores, *Annu. Rev. Mater. Sci.*, *1*, 43–63, doi:10.1146/annurev.marine.010908.163712.

Xie, P. P., and P. A. Arkin (1996), Analyses of global monthly precipitation using gauge observations, satellite estimates, and numerical model predictions, *J. Clim.*, *9*(4), 840–858, doi:10.1175/1520-0442(1996)009<0840:AOGMPU>2.0.CO;2.

Yasuda, I., Y. Hiroe, K. Komatsu, K. Kawasaki, T. M. Joyce, F. Bahr, and Y. Kawasaki (2001), Hydrographic structure and transport of the Oyashio south of Hokkaido and the formation of North Pacific Intermediate Water, *J. Geophys. Res.*, *106*(C4), 6931–6942, doi:10.1029/1999JC000154.

Yeager, S. G., and M. Jochum (2009), The connection between Labrador Sea buoyancy loss, deep western boundary current strength, and Gulf Stream path in an ocean circulation model, *Ocean Modell.*, *30*(2–3), 207–224, doi:10.1016/j.ocemod.2009.06.014.

Zhang, Y. C., W. B. Rossow, A. A. Lacis, V. Oinas, and M. I. Mishchenko (2004), Calculation of radiative fluxes from the surface to top of atmosphere based on ISCCP and other global data sets: Refinements of the radiative transfer model and the input data, *J. Geophys. Res.*, *109*, D19105, doi:10.1029/2003JD004457.

F. O. Bryan, K. Lindsay, and K. Misumi, Climate and Global Dynamics Division, National Center for Atmospheric Research, PO Box 3000, Boulder, CO 80307-3000, USA. (misumi@ucar.edu)

S. C. Doney, Department of Marine Chemistry and Geochemistry, Woods Hole Oceanographic Institution, 266 Woods Hole Rd., MS 25, Woods Hole, MA 02543, USA.

H. Mitsudera, T. Nakamura, J. Nishioka, and K. Uchimoto, Pan-Okhotsk Research Center, Institute of Low Temperature Science, Hokkaido University, Kita-19, Nishi-8, Kita-ku, Sapporo, Hokkaido 060-0819, Japan.

J. K. Moore, Department of Earth System Science, University of California, 3214 Croul Hall, Irvine, CA 92697-3100, USA.

D. Tsumune and Y. Yoshida, Environmental Science Research Laboratory, Central Research Institute of Electric Power Industry, 1646 Abiko, Abiko, Chiba 270-1194, Japan.